



저작자표시-비영리-변경금지 2.0 대한민국

이용자는 아래의 조건을 따르는 경우에 한하여 자유롭게

- 이 저작물을 복제, 배포, 전송, 전시, 공연 및 방송할 수 있습니다.

다음과 같은 조건을 따라야 합니다:



저작자표시. 귀하는 원저작자를 표시하여야 합니다.



비영리. 귀하는 이 저작물을 영리 목적으로 이용할 수 없습니다.



변경금지. 귀하는 이 저작물을 개작, 변형 또는 가공할 수 없습니다.

- 귀하는, 이 저작물의 재이용이나 배포의 경우, 이 저작물에 적용된 이용허락조건을 명확하게 나타내어야 합니다.
- 저작권자로부터 별도의 허가를 받으면 이러한 조건들은 적용되지 않습니다.

저작권법에 따른 이용자의 권리는 위의 내용에 의하여 영향을 받지 않습니다.

이것은 [이용허락규약\(Legal Code\)](#)을 이해하기 쉽게 요약한 것입니다.

[Disclaimer](#)

약학 석사 학위논문

**Structural and functional studies on
PemIK toxin-antitoxin system from
*Staphylococcus aureus***

Staphylococcus aureus 유래 PemIK TA system
단백질 복합체의 구조 및 기능 연구

2022년 8월

서울대학교 대학원

약학과 약학전공

백성민

**Structural and functional studies on
PemIK toxin-antitoxin system from
*Staphylococcus aureus***

지도 교수 이 봉 진

이 논문을 석사 학위논문으로 제출함

2022년 5월

서울대학교 대학원

약학과 약학전공

백 성 민

백성민의 석사 학위논문을 인준함

2022년 8월

위 원 장 _____ 변 영 로 (인)

부위원장 _____ 오 유 경 (인)

위 원 _____ 이 봉 진 (인)

Abstract

Structural and functional studies on PemIK toxin-antitoxin system from *Staphylococcus aureus*

Sung-Min Baek

College of pharmacy

Seoul National University

Staphylococcus aureus is a notorious and globally distributed pathogenic bacterium. Especially, the emergence of methicillin-resistant *S. aureus* (MRSA) along with the widespread use of different classes of antibiotics has become a significant therapeutic challenge. Antibiotic resistance is a disturbing problem that poses a threat to humans. New strategies to develop novel antibiotics based on intrinsic bacterial toxin–antitoxin (TA) systems have been recently reported. Because TA systems are present only in bacteria and not in humans, these distinctive systems are attractive targets for developing antibiotics with new modes of action. *S. aureus* PemIK is a type II TA system, comprising the toxin protein PemK and the labile antitoxin protein PemI. Here, we determined the crystal structures of both PemK and the PemIK complex, in which PemK is neutralized by PemI. Our biochemical approaches, including fluorescence quenching and polarization assays, identified Glu20, Arg25, Thr48, Thr49, and Arg84 of PemK as

being important for RNase function. Our study indicates that the active site and RNA-binding residues of PemK are covered by PemI, leading to unique conformational changes in PemK accompanied by repositioning of the loop between 1and2. These changes can interfere with RNA binding by PemK. Overall, PemK adopts particular open and closed forms for precise neutralization by PemI. This structural and functional information on PemIK will contribute to the discovery and development of novel antibiotics in the form of peptides or small molecules inhibiting direct binding between PemI and PemK.

Keyword : Staphylococcus aureus, Antibiotic resistance, Toxin-antitoxin system, PemIK, X-ray crystallography, conformational change

Student Number : 2020-28855

Table of Contents

Chapter 1. Introduction	4
Chapter 2. Materials and Methods	6
2.1 Gene cloning	6
2.2 Protein Expression and purification	6
2.3 Crystallization and X-ray data collection	8
2.4 Structure determination and refinement	9
2.5 Size-exclusion chromatography with multiangle light scattering (SEC-MALS).....	10
2.6 Fluorescence polarization (FP) assay.....	10
2.7 <i>In vitro</i> RNase activity assay.....	11
2.8 Molecular dynamics (MD) simulation.....	11
Chapter 3. Results and Discussions.....	13
3.1 Structural analysis of the <i>S. aureus</i> PemK	13
3.2 Structural comparison of <i>S. aureus</i> PemK with its homologs.....	17
3.3 <i>S. aureus</i> PemK shows RNA-binding and RNase activities.....	20
3.4 The <i>S. aureus</i> PemI monomer neutralizes the PemK dimer by forming a structural complex.....	24
3.5 Loop L12 in PemK plays a decisive role in the formation of the PemIK complex	26
Chapter 4. Conclusions.....	30
Reference	33
Abstract in Korean.....	41

Chapter 1. Introduction

Toxin-antitoxin (TA) systems are modules that comprise a set of genes encoding a toxin and an antitoxin. The first TA system was discovered in the *Escherichia coli* F plasmid (1). The plasmid addiction module produces a stable antibacterial toxin that impairs an essential cellular process and a labile antitoxin that neutralizes the deleterious activity of the toxin (2). However, in plasmid-free cells, both toxins and antitoxins are not replenished, and the antitoxin is degraded more rapidly by the host enzyme than the toxin. Eventually, the remaining free toxin triggers death or growth arrest of the cell (2,3). Later, it was discovered that many TA systems also exist in bacterial chromosomes, in addition to plasmids. Recently, based on regulatory roles in the virulence and survival of bacteria under stress conditions, TA systems have been considered to be attractive targets for the development of novel antibiotics (4-6).

TA systems have been classified into six types according to the mode of actions and the nature of antitoxins: the proteins are classified as type II, IV, V, or VI, whereas the RNAs are classified as type I or III (7). In the type II system, toxins generally exhibit ribonuclease (RNase) activities and are further classified according to ribosomal dependency (8), cellular target (9), and mode of action (9,10).

Although TA systems are widespread among bacteria, *Staphylococcus aureus* carries fewer type II TA system components than other species, such as *Mycobacterium tuberculosis* and *E. coli* (11,12). To date, three kinds of type II TA pairs have been experimentally verified in *S. aureus*, namely, MazEF/PemIK, YefM-YoeB (AxeTxe), and Omega-Epsilon-Zeta (13-15). Among them, MazEF is one of the extensively characterized TA systems (14). The toxin MazF dimer is an RNase that specifically cleaves the mRNA sequence UACAU in a ribosome-independent manner. It forms the hexameric MazF₂-MazE₂-MazF₂ complex by binding to the antitoxin MazE dimer.

In *S. aureus* CH91, plasmid emergency maintenance inhibitor or killing (PemIK) (16) was discovered as a novel type II TA system (17). The pemIK locus is encoded by a 17-kb plasmid (pCH91) of *S. aureus* CH91 that contains genes related to virulence factors and plasmid stability (18,19). The toxin PemK, as an endoribonuclease, specifically recognizes and cleaves the tetrad sequence U↓AUU in a target mRNA in a ribosome-independent manner (20). The antitoxin PemI is hypothesized to perform dual actions of a transcription factor and a neutralizer of toxin activity, which also allows bacterial survival. Interestingly, the target sequence (U↓AUU) of PemK is found in a considerable number of mRNA transcripts encoding proteins involved in virulence but not in the cell translation machinery (17,21-24). Additionally, *S. aureus* PemK affected protein regulation in *Caenorhabditis elegans*, which is a relevant model of higher eukaryotes, according to the research by Mir *et al.* (25). The regulated proteins were involved in ATP generation, protein synthesis, lipid synthesis, cytoskeleton function, heat shock response, innate immune defense, stress response, neuron degeneration, muscle assembly, and so on. Regarding the other pathogenic bacteria, including *Klebsiella pneumoniae*, *Bacillus anthracis* and *Mycobacterium tuberculosis*, overexpression of the PemK gene led to the severe inhibition of bacterial growth (26-28). PemK toxins modulate specific gene pools of the bacterial transcriptome in an orchestrated manner but remain elusive at the experimental level (28). Despite these roles of PemIK as a global virulence modulator in *S. aureus*, the structure and function of *S. aureus* PemIK remain unknown.

In this study, we determined the crystal structures of both *S. aureus* PemK and PemI-neutralized PemK. The structures demonstrate an RNase SH3-like fold for PemK and PemI-induced conformational changes in PemK. Biophysical and biochemical analyses with mutagenesis experiments have revealed the key residues for the activity of *S. aureus* PemK. These results provide a structural basis for understanding the molecular function of PemIK and a platform for the discovery of novel antibiotics.

Chapter 2. Materials and Methods

2.1. Gene cloning

The genes encoding PemK and PemI from plasmid pCH91, which was isolated from *S. aureus* CH-91 (29), were synthesized by Bioneer (Daejeon, Korea) and PCR-amplified using the following pairs of oligonucleotides: The forward/reverse oligonucleotide primers for PemK were PemK-F/PemK-R; for crystallization of the PemIK complex, a truncated PemI construct encompassing Lys57 to Ile89 was introduced, and the PemI-F/PemI-R primer pair was used for PCR. The PCR products were digested with *NdeI* and *XhoI*. The PemK gene was ligated into *NdeI-XhoI*-digested pET-28b(+) (Novagen, Madison, WI, USA), resulting in a twenty-residue tag (MGSSHHHHHSSGLVPRGSH) being added to the amino terminus of the recombinant protein. We also generated PemI constructs by cloning the gene into *NdeI-XhoI*-digested pET-21a(+) (Novagen). The resulting plasmids were transformed into *E. coli* strain DH5 α for amplification.

To identify the residues essential for the RNase activity of PemK, we mutated the Glu20, Arg25, Thr48, Thr49, and Arg84 residues to Ala by using the EZchangeTM Site-Directed Mutagenesis Kit (Enzymomics, Daejeon, Korea) according to the manufacturer's protocol.

2.2. Protein expression and purification

The recombinant PemK protein was overexpressed in *E. coli* Rossetta2(DE3) cells using Luria-Bertani culture medium. PemK expression was induced by 0.75 mM isopropyl 1-thio- β -D-galactopyranoside (IPTG), and the cells were incubated for an additional 2 h and 30 min at 37°C following growth to mid-log phase at 37°C. The cells were harvested by centrifugation at 6,300 \times g and frozen at -80°C.

The harvested cells were resuspended in buffer A (20 mM Tris-HCl, pH 7.9, and 500 mM NaCl) containing 5% (v/v) glycerol and lysed by ultrasonication. After centrifugation at 28,300 \times g for 1 h at 4°C, the supernatant containing the PemK protein was loaded on an open Ni²⁺-NTA column (Qiagen, Hilden, Germany) pre-equilibrated with buffer A and washed with buffer A containing 100 mM imidazole. The protein bound to the column resin was eluted by an imidazole gradient (100–500 mM). The final purification step was size exclusion chromatography on a HiLoad 16/60 Superdex 200 prep-grade column (GE Healthcare, Chicago, IL, USA) in a buffer containing 50 mM Tris-HCl, pH 7.9, and 150 mM NaCl. Fractions containing PemK were pooled and concentrated to 11 mg/ml using an Amicon Ultra centrifugal filter unit (Merck Millipore, Burlington, MA, USA) for crystallization. The purity of PemK was confirmed by SDS-PAGE.

For co-expression of PemK and PemI, both plasmids, namely, PemK cloned in pET28b(+) with an N-terminal poly-His-tag and PemI cloned in pET21a(+) with no tag, were co-transformed into *E. coli* BL21(DE3), and the cells were spread on an agar plate containing both ampicillin and kanamycin. *E. coli* BL21(DE3) cells harbouring the PemIK complex protein were grown in Luria-Bertani culture medium with ampicillin and kanamycin until the OD₆₀₀ reached 0.5–0.6 at 37°C, and protein overexpression was induced by the addition of 0.5 mM IPTG. The purification procedure used for PemK was also used to purify the PemIK protein complex. The PemIK complex labelled with selenomethionine (SeMet) was obtained by the same procedure, except that cells containing the SeMet-labelled PemIK complex were grown in M9 medium containing extra essential amino acids.

For the NMR experiments, the PemK protein was overexpressed using M9 culture medium supplemented with 1.0 g/l [U-¹³C] glucose and 1.0 g/l [¹⁵N] NH₄Cl (Cambridge Isotopes Laboratories, Tewksbury, MA, USA) as the sole carbon and nitrogen sources, respectively. To perform NMR experiments, the target proteins were purified by procedures identical to those described above except that size exclusion chromatography on a HiLoad 16/60 Superdex 200 prep-grade column

(GE Healthcare) was conducted in buffer containing 20 mM Bis-Tris, pH 6.5, and 100 mM NaCl.

2.3. Crystallization and X-ray data collection

Crystals of PemK were grown using the sitting-drop vapor diffusion method at 20°C by mixing equal volumes (0.5 μ l each) of the protein solution (at 11 mg/ml concentration) and the reservoir solution consisting of 20% (w/v) PEG 1000, 0.1 M potassium phosphate monobasic/sodium phosphate dibasic, pH 6.2, and 0.2 M sodium chloride. Prior to data collection, a cryoprotectant solution consisting of 20% (v/v) glycerol added to the reservoir solution was used. The crystal was vitrified in a cold nitrogen gas stream, and the data were collected using a Quantum-210 CCD detector (ADSC, Poway, CA, USA) at beamline AR-NW12A of Photon Factory, Japan. The crystals of PemK belonged to the monoclinic space group $P2_1$, with unit cell parameters of $a = 56.25 \text{ \AA}$, $b = 61.42 \text{ \AA}$, $c = 75.51 \text{ \AA}$, $\alpha = \gamma = 90.00^\circ$, and $\beta = 101.20^\circ$.

SeMet-labelled PemIK complex crystals were grown using the sitting-drop vapor diffusion method at 20°C by mixing equal volumes (0.5 μ l each) of the protein solution (at 20 mg/ml) and the reservoir solution consisting of 2.0 M ammonium sulfate, 100 mM CAPS/sodium hydroxide, pH 10.5 and 200 mM lithium sulfate. Crystals were soaked in a cryoprotectant solution [the reservoir solution with 20% (v/v) glycerol]. Data collection for the SeMet-labelled PemIK complex was conducted on a Quantum-315 CCD detector (ADSC) at beamline 5C of Pohang Accelerator Laboratory, Korea. The crystal of the SeMet-labelled PemIK complex belonged to the cubic space group $F4_132$, with unit cell parameters of $a = b = c = 266.43 \text{ \AA}$ and $\alpha = \beta = \gamma = 90.0^\circ$. The crystallization procedure for native PemIK was the same as that for SeMet-labelled PemIK. Data collection for the native PemIK complex crystals was conducted on an EIGER 16M CCD detector (DECTRIS, Philadelphia, PA, USA) at beamline BL44XU of Spring-8, Japan. The

crystal of the native PemIK complex belonged to tetragonal space group $I4_122$, with unit cell parameters of $a = b = 164.51 \text{ \AA}$, $c = 232.21 \text{ \AA}$, and $\alpha = \beta = \gamma = 90.00^\circ$.

Raw data were processed and scaled using the *HKL2000* (30) and *XDS* (31) program packages. The statistics for each data point are summarized in Table 1.

2.4. Structure determination and refinement

The PemK structure was solved by the molecular replacement method using the program Phaser-MR (32) with a monomer model of *E. coli* Kid (PDB code 1M1F) (33) used as the starting model at a resolution of 1.94 \AA . A set of single-wavelength anomalous dispersion data from a crystal of the SeMet-labelled PemIK complex was used to solve the phase problem at a resolution of 2.8 \AA . Phase calculation, density modification, and initial model building for the complex were conducted using *Autosol* and *AutoBuild* of *PHENIX Program suite* (34). The structures of PemK and the PemIK complex were refined at resolutions of 1.94 \AA and 2.00 \AA , respectively. Five percent of the data were randomly set aside as the test set for calculating R_{free} for all data (35). The models were manually modified using the program *Coot* (36) and refined with the programs *Refmac* in *CCP4 Program suite* (37,38) and *phenix.refine* in *PHENIX* (34), including bulk solvent correction. Water molecules and ligands were added using the program *Coot* (36) and were manually inspected. The stereochemistry of all models was evaluated by the program *MolProbity* (39). Interface areas and the interactions involved were calculated using *PISA* (40) and Protein Interactions Calculator (*PIC*) (41). Visualization of the structures was conducted using the program *PyMOL* (PyMOL Molecular Graphics System, version 2.0.6; Schrödinger, LLC., Cambridge, MA, USA).

2.5. Size-exclusion chromatography with multiangle light scattering (SEC-MALS)

To determine the oligomeric states of the wild-type PemK (WT) and mutants (E20A and R84A), SEC-MALS experiments were conducted using a fast protein liquid chromatography (FPLC) system (Cytiva, Marlborough, MA, USA) connected to a MiniDAWN TREOS MALS instrument (Wyatt, Santa Barbara, CA, USA). A Superdex 75 10/300 GL (Cytiva) gel filtration column was pre-equilibrated with a buffer (50 mM Tris, pH 7.9, and 150 mM NaCl). Detector normalization was achieved using 2 mg/ml Bovine Serum Albumin (Thermo Fisher Scientific, Waltham, MA, USA). 200 μ l of proteins were injected at a concentration of 2 mg/ml. The data were analyzed using the ASTRA 8 software (Wyatt).

2.6. Fluorescence polarization (FP) assay

Serially diluted PemK and 40 nM 5'-FAM-labelled ssRNA probe (Bioneer) in a final volume of 50 μ l were incubated at room temperature for 20 minutes in a buffer containing 50 mM Tris, pH 7.9, and 150 mM NaCl. All experiments were performed in triplicate. Fluorescence polarization (FP) was analyzed using a SpectraMax M5 plate reader (Molecular Devices, San Jose, CA, USA) by measuring the parallel fluorescence emission (F_{\parallel}) and perpendicular fluorescence emission (F_{\perp}) at 530 nm (excitation at 485 nm), and the FP value was calculated using Equation 1. To calculate K_d values, non-linear regression was used to fit the anisotropy data (y) as a function of total protein concentration (x) by *KaleidaGraph* software (Synergy Software, Reading, PA, USA) according to Equation 2 (44), where m_1 and m_2 are the minimum and maximum anisotropy values, respectively, and m_3 is the K_d value.

$$\text{Equation 1} \quad \text{FP (mP)} = 1000 \times \frac{F_{-} - G \cdot F_{\perp}}{F_{-} + G \cdot F_{\perp}}$$

$$\text{Equation 2} \quad y = m_1 + (m_2 - m_1) \times \frac{x}{m_3 + x}$$

2.7. *In vitro* RNase activity assay

To monitor the RNase activity of PemK, a fluorescence quenching assay was conducted on the WT PemK and its mutants using the RNase Alert Kit (IDT, Coralville, IA, USA) at 37 °C for 30 min. The assays were performed in a buffer containing 20 mM Tris, pH 7.5, and 150 mM NaCl. The 20 μ l of reaction mixture contained 0.35 μ M PemK (WT or mutants) with an RNA concentration range of 0.1–2.0 μ M. A fluorophore covalently attached to a synthetic RNA strand was quenched by a quencher group attached to the other end. When the RNA was digested by an RNase, the fluorophore was released from the quencher. The released fluorophore emitted fluorescence at 520 nm upon excitation at 490 nm. The fluorescence was measured as RFU on a SpectraMax M5 plate reader (Molecular Devices). Michaelis–Menten kinetics was used to analyze the initial velocities and kinetic parameters K_m and k_{cat} using *KaleidaGraph* software (Synergy Software).

2.8. Molecular dynamics (MD) simulation

To study the RNA recognition and PemI binding of PemK, triplicate runs of 300 ns MD simulations for three kinds of structures, PemK, PemIK, and ssRNA-bound PemK, were conducted. Three protein models were prepared using Protein Preparation Wizard (47) in Schrödinger suite. All MD simulations were conducted using Desmond (48) in Schrödinger suite 2020-4. For explicit solvent simulations, the periodic boundary condition using orthorhombic box at $10 \times 10 \times 10$ Å distances was applied. The system was solvated with water adopting the TIP3P water model and 150 mM NaCl after it was electrically neutralized with sodium (or

chloride) ions. The solvated system was energy-minimized and relaxed for 100 ps using the minimization step of Desmond with OPLS2005 force field (49). MD simulations were performed in the NPT (isothermal and isobaric simulation) ensemble, where Martyna-Tobias-Klein method (50) and Nose-Hoover thermostat algorithm (51) were used for isotropic pressure (1 atm) and constant temperature (300 K), respectively. Total 300 ns simulations for PemK, PemI-neutralized PemK, and ssRNA-bound PemK were run and saved as trajectories at 300 ps intervals with three independent replicates. The trajectories were analyzed using Simulation Event Analysis and Simulation Interaction Diagram in Desmond.

Chapter 3. Results and Discussions

3.1. Structural analysis of the *S. aureus* PemK

Our initial approach included determination of the PemIK complex structure, involving successful solubilization, purification, and structural analysis of the PemIK complex and PemK. Before acquiring the PemIK complex structure, we obtained the structure of the toxin protein PemK at a resolution of 1.94 Å. The refined model of PemK accounts for four monomers, which form two dimers (A/B chains and C/D chains), with four phosphate ions and one glycerol in the asymmetric unit (Figure 1A). The refinement statistics are summarized in Table 1. Each monomer of PemK exhibits pair-wise backbone root mean square deviations (RMSDs) of 0.09–0.31 Å for 110–111 C α atom pairs. PemK adopts an SH3-like barrel fold consisting of a seven-stranded, twisted, antiparallel β -sheet in the order β 7- β 1- β 2- β 3- β 5/ β 6- β 4 and surrounded by two α -helices (α 1 and α 2) (Figure 1B).

The interface areas among the four monomers (chains A–D) in the PemK structure indicate that two stable dimers (dimers A/B and C/D) exist in the asymmetric unit. The interface area between chains A and B (or between C and D) is 1,723 Å² (or 1,712 Å²) for the PemK dimers, while the interface area of the other possible pairs A/C, A/D, B/C, and B/D are 288, 0, 406, 277 Å², respectively. The dimeric structures of the PemK crystals were in good agreement with the SEC-MALS results, which showed the dimeric forms in solution. In the dimerization interfaces of PemK (chains A/B and chains C/D), hydrophilic and hydrophobic interactions are present, as shown in Figure 1C. Residues on α 1, α 2, β 3, L12, L56, and L67 are mainly involved in the formation of the dimeric interface. L12, L56, and L67 are the loops in β 1/ β 2, β 5/ β 6, and β 6/ β 7, respectively. Eighteen residues are related to hydrophilic interactions, namely, Gln5, Arg19, Glu20, Asn32, Gln33, Met34, Thr39, Trp43, Val74, Ile76, Ala78, Asp80, Arg84, Thr106, Tyr107, Leu108,

Lys109, and Thr111. All of the hydrophilic interactions are hydrogen bonds. Ten residues contribute to hydrophobic interactions, namely, Pro15, Phe41, Trp43, Val74, Ile76, Leu101, Ile104, Tyr107, Leu108, and Pro110. Among the residues in the dimerization interfaces, Arg19, Glu20, Asp80, and Arg84 interact with each other and neighboring residues via strong and extensive hydrophilic interactions (Figure 1C). However, E20A and R84A mutations did not principally cause dissociation of PemK dimer as shown in SEC-MALS. The four residues are positioned in two loops (Arg19 and Asp20 in L12; Asp80 and Arg84 in L67). These two loops may play important roles in complexes with either RNA or the cognate antitoxin PemI, which can be accompanied by the movement of two loops, especially in the case of PemI binding (details are discussed in the section titled ‘L12 in PemK play a decisive role in the formation of the PemIK complex’).

Table1. Statistics for data collection and model refinement

Dataset	PemK	PemIK SeMet	PemIK
Data collection			
Wavelength (Å)	1.0000	0.9795	0.9000
Space group	P 2 ₁	F 4 ₁ 3 2	I 4 ₁ 2 2
Cell dimensions			
<i>a, b, c</i> (Å)	56.25, 61.42 75.51	266.43, 266.43, 266.43	164.51, 164.51, 232.21
α, β, γ (°)	90.00, 101.20, 90.00	90.00, 90.00, 90.00	90.00, 90.00, 90.00
Resolution range (Å)	40.00–1.94 (1.97– 1.94)	50.00–2.62 (2.67– 2.62)	50.00–2.00 (2.12– 2.00)
Total/unique reflections	150,418/37,045	1,074,093/45,479	1,465,174 /205,519
Completeness (%)	97.4 (79.8)	100.0 (100.0)	99.8 (98.9)
Redundancy	4.1 (3.6)	23.6 (24.3)	7.1 (6.7)
<i>R</i> _{merge} (%) ^a	10.5 (46.1)	29.2 (100)	5.7 (76.3)
Mean <i>I</i> / σ (<i>I</i>)	24.1 (3.8)	35.8 (5.2)	19.5 (2.2)
CC _{1/2}	0.988 (0.877)	0.973 (0.900)	1.000 (0.789)
Refinement			
Resolution range (Å)	33.95–1.94		38.77–2.00

$R_{\text{work}}/R_{\text{free}}^b$	20.26/23.96	18.77/21.88
r.m.s. deviations		
Bond lengths (Å)	0.009	0.018
Bond angles (°)	1.237	1.649
Number of atoms / Average B-factors (Å ²)		
Protein	3,639 / 24.9	6,275 / 44.4
Glycerol	6 / 26.5	6 / 44.9
Phosphate ion	20 / 29.1	
Sulfate ion		65 / 49.7
Water	371 / 33.8	515 / 52.8
Ramachandran plot ^c		
Most favored (%)	96.12	97.32
Allowed (%)	3.88	2.67
Outliers (%)	0.00	0.00
Rotamer outliers	0.00	0.00
PDB accession code	7EWI	7EWJ

^a $R_{\text{merge}} = \sum_h \sum_i |I(h)_i - \langle I(h) \rangle| / \sum_h \sum_i I(h)_i$, where $I(h)$ is the intensity of reflection h , \sum_h is the sum over all reflections, and \sum_i is the sum over i measurements of reflection h .

^b $R = \sum | |F_{\text{obs}}| - |F_{\text{calc}}| | / \sum |F_{\text{obs}}|$, where R_{free} is calculated for a randomly chosen 5% of reflections, which were not used for structure refinement and R_{work} is calculated for the remaining reflections.

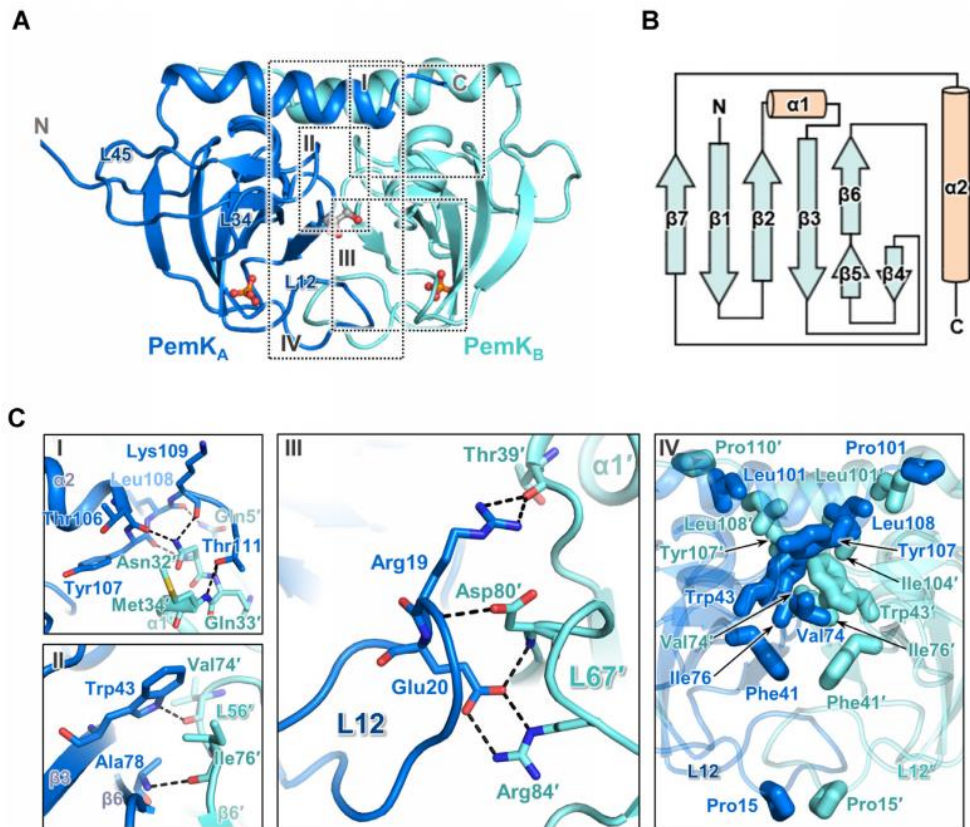


Figure 1. Overall structure of PemK. (A) Overall structure of the PemK dimer. Chains A and B are represented in blue and cyan, respectively. Phosphate ions (orange) and a glycerol molecule (grey) are shown in ball and stick representation, respectively. The regions depicted in (C) are marked as squares with each label. (B) Diagram of the secondary structure of the PemK monomer. The PemK monomer consists of two α -helices and seven β -strands forming SH-like barrel folds. α -Helices and β -strands are colored light orange and cyan, respectively. (C) Dimerization of PemK. The regions containing hydrogen bonds in the PemK dimer are shown in I, II, and III. The residues involved in hydrophobic interactions are represented in IV.

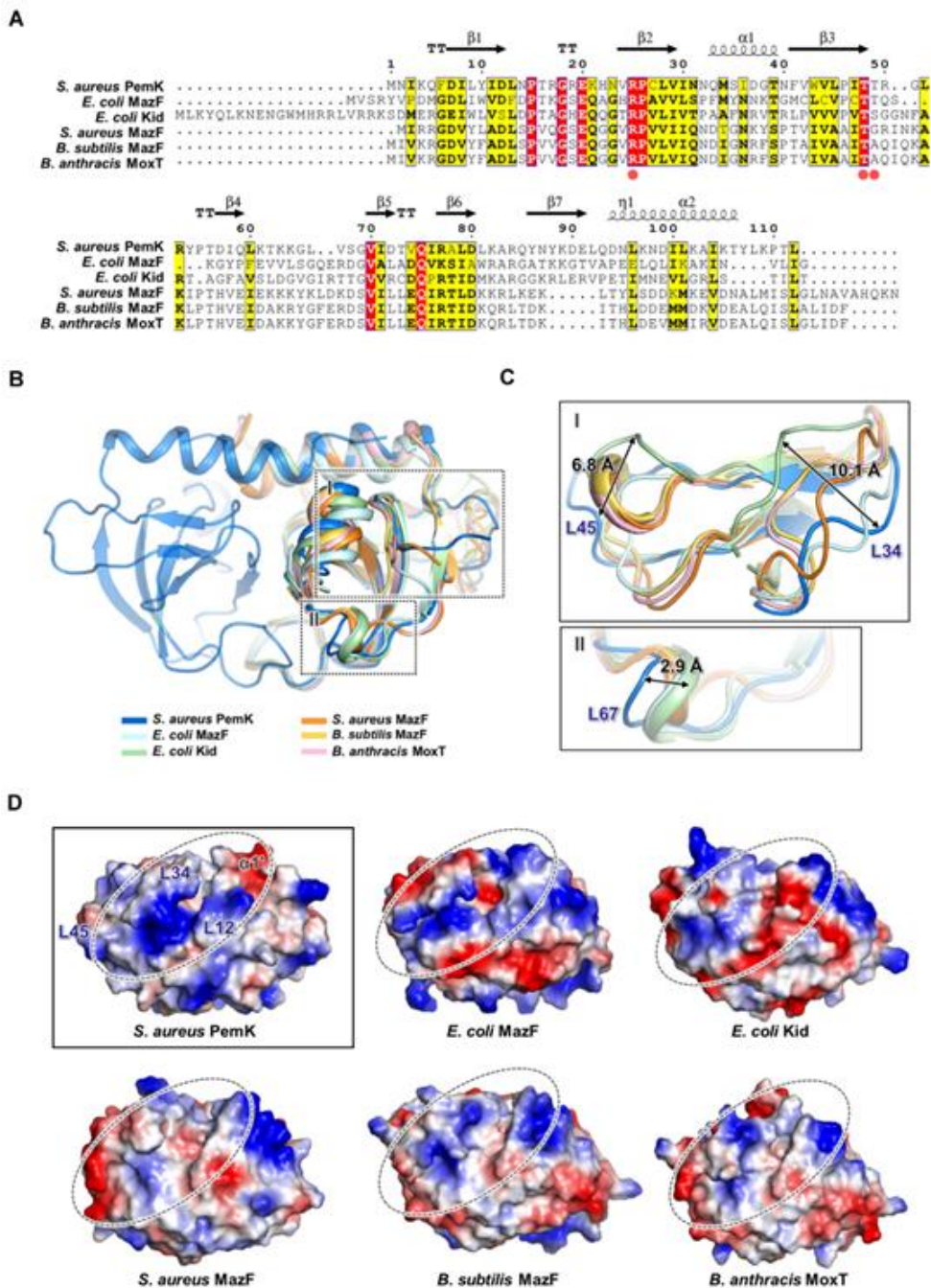
3.2. Structural comparison of *S. aureus* PemK with its homologs

When the *S. aureus* PemK structure was compared with those of its homologs using the Dali server (2), *E. coli* MazF (PDB code 5CR2) (49) showed the highest structural similarity with PemK, showing Z-scores of 16.4–16.7. The next highest Z-score was 16.6, acquired from *E. coli* Kid (PDB code 1M1F) (33). *S. aureus* MazF (PDB code 4MZM) (50) and *B. subtilis* MazF (PDB code 4MDX) (46) also displayed similar Z-scores, with values of 15.5–15.8 and 15.6–15.8, respectively. The structure of PemK also shared similarity with that of *B. anthracis* MoxT (PDB code 4HKE) (51).

Although PemK and its homologs share conserved residues, as shown by sequence alignment (Figure 2A), and exhibit similar folds (Figure 2B), differences in secondary structures exist among them. The long loop between $\beta 1$ and $\beta 2$ (L12) plays an essential role in controlling the PemI or RNA binding. In the PemK dimer, L12s are held by each other via the formation of hydrogen bonds with L67 like a gate, which gives aid to RNA binding. Interestingly, L12 controls the binding of the antitoxin PemI, as described later. The loop between $\beta 3$ and $\beta 4$ (L34) and the loop between $\beta 4$ and $\beta 5$ (L45) also show large C α RMSDs of 10.1 and 6.8 Å for residues Arg53 and Gly65, respectively, compared to the equivalent segments in *E. coli* Kid (Figure 2C). L34 of PemK faces L12. Some homologs, such as *Bacillus anthracis* MoxT and *B. subtilis* MazF, have 3_{10} -helices instead of the loop. Additionally, most homologs have 3_{10} -helices in the region corresponding to L67, except *E. coli* MazF and PemK.

The structures of MazF from *B. subtilis* and *E. coli* were bound to RNA and DNA analogs, respectively. The nucleotide-binding region was composed of the interface between L12 and L34 of one monomer and $\alpha 1$ of the other monomer. The electrostatic potential surface of the predicted nucleotide-binding region in *S. aureus* PemK also exhibited differences compared to those in the homologs (Figure

2D). Most homologs possessed crevices in the interfaces between monomers, corresponding to L12 and L34 of the *S. aureus* PemK dimers. In particular, *S. aureus* PemK has a distinct positively charged patch in this region in contrast to the other homologs. Additionally, the difference in the loop lengths of L12 and L34 makes the crevice of *S. aureus* PemK dissimilar to those of the homologs. The distinctive structural dissimilarity of *S. aureus* PemK may be related to determinants for the mRNA sequences. We observed that structures of L34 and L45 are not affected by crystal packing in both PemK and PemIK complex structures.



were conducted using Clustal Omega (61) and ESPript 3.0 (62). (B) Overlay structure of PemK with other homologs. *S. aureus* PemK (light blue), *E. coli* MazF (cyan), *E. coli* Kid (light green), *S. aureus* MazF (orange), *B. subtilis* MazF (yellow), and *B. anthracis* MoxT (pink) are shown. (C) Loop regions of PemK and its homologs. The regions exhibiting distinct features in (B) are shown in boxes I and II. (D) Electrostatic surface potential represents different charge distributions between the L34 and L12 regions in PemK and its homologs. The positive crevice regions are highlighted in dotted circles.

3.3. *S. aureus* PemK shows RNA-binding and RNase activities

The crystal structure of the toxin protein PemK was obtained in phosphate ion-bound form. The structures show that residues Arg25 in β 2, Thr48 in β 3, and Thr49 in L34 form hydrogen bonds with phosphate ions between L12 and L34, which are adjacent to the putative active site (Figure 3A). Interestingly, structural superimposition of *S. aureus* PemK with sulfate ion-bound *B. anthracis* MoxT (PDB code 4HKE) (51) and phosphate ion-bound *E. coli* Kid (PDB cod 1M1F) (33) revealed that the coordinate of the phosphate ion in *S. aureus* PemK is identical to those of the sulfate ion in *B. anthracis* MoxT and phosphate ion in *E. coli* Kid (Figure 3B). Overlay with the structure of RNA-bound MazF from *B. subtilis* (PDB code 4MDX) (46) showed that the negatively charged phosphate ion of *S. aureus* PemK matched the scissile phosphate between dU3 and A4 of the bound RNA in the *B. subtilis* MazF structure (Figure 3C). The residues involved in the interactions are also similar between the two structures. These insights indicate that this location is the possible active site of PemK.

It is known that the toxin PemK plays a role as a ribosome-independent RNase that recognizes a specific sequence, U↓AUU (17). To investigate the residues that contribute to the RNase activity of PemK, point mutagenesis of PemK

was conducted. For this purpose, we mutated residues Arg25, Thr48, and Thr49, which form hydrogen bonds with a phosphate ion, to Ala. Because Arg84 is also considered a key residue (17), the hydrogen bond pairing residue Glu20 was mutated to Ala. Using these mutants, a fluorescence quenching assay was carried out to determine the effects of the mutations on RNase activity in the potential active site of PemK. As shown in Figure 4A, all of the mutants led to the detectable loss in RNase activity. The mutants exhibited about ~40-60 % reduced RNase activity. The K_m and k_{cat} values of the WT PemK were 0.65 μM and 13.0 $\text{RFU min}^{-1} \mu\text{M}^{-1}$, respectively. All of the mutants showed increased K_m values and decreased k_{cat} values, compared to those of the WT PemK, which indicates all of the mutants might be involved in catalytic activity. The mutant enzymes show reduced efficiencies with 1.5-fold to 3.3-fold decreased k_{cat}/K_m . The mutation of Arg25 and show increases of K_m by 1.1- to 1.8-folds and decreases of k_{cat} to 1.3-folds, while E20A, T48A, and R84A mutants exert > 3-folds increases of K_m and minor decreases of k_{cat} values. The data analyzed using Michaelis–Menten kinetics are summarized in Table 2.

Additionally, we measured the RNA-binding ability of PemK (WT) and its mutants (E20A, R25A, T48A, T49A, and R84A) using an FP assay (Figure 4B). As mentioned above, these five mutants showed reduced RNase activity. The FP assay with an uncleavable 8-mer ssRNA showed that mutation of R25A and R84A led to 25- to 30-fold weaker RNA-binding ability than that of the WT protein. The E20A and T48A mutant showed 3.9- to 6.5-fold reduction in RNA-binding affinity. In contrast, mutation of Thr49 to Ala led to a similar affinity for the RNA substrate as that of the WT protein. In PemK, we found that E20A, Arg25, Thr48, and Arg84 are key residues for RNA-binding and catalytic activities.

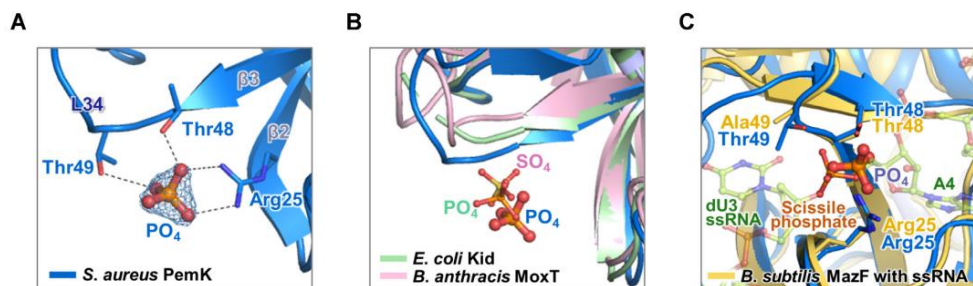


Figure 3. Active site of PemK and its homologs. (A) Putative active site of PemK. The $2Fo-Fc$ electron density map contoured at 1.5σ around PO_4 was drawn with the model. The hydrogen bonds between PO_4 and the putative active site residues Arg25, Thr48, and Thr49 are depicted as dashed grey lines. (B) PO_4 of *E. coli* Kid and SO_4 of *B. anthracis* MoxT are overlaid with PO_4 of *S. aureus* PemK. (C) Overlay of *S. aureus* PemK and *B. subtilis* MazF with ssRNA. The position of the scissile phosphate of ssRNA in *B. subtilis* MazF was well matched with the position of PO_4 in *S. aureus* PemK.

Table 2. Comparison of kinetic parameters of WT and mutants of PemK

PemK	k_{cat}^a	K_m^a	K_{cat} / K_m
WT	13.00	0.65	20.0
E20A	12.62	$> 2.0^b$	$< 6.31^b$
R25A	9.80	0.74	13.24
T48A	12.39	$> 2.0^b$	$< 6.20^b$
T49A	9.96	1.22	8.16
R84A	12.05	$> 2.0^b$	$< 6.03^b$

^a The units of K_{cat} and K_m are defined as $RFU \text{ min}^{-1} \mu\text{M}^{-1}$ and μM , respectively.

^b Due to the solubility of RNA substrates, accurate values of K_m and K_{cat} / K_m cannot be determined.

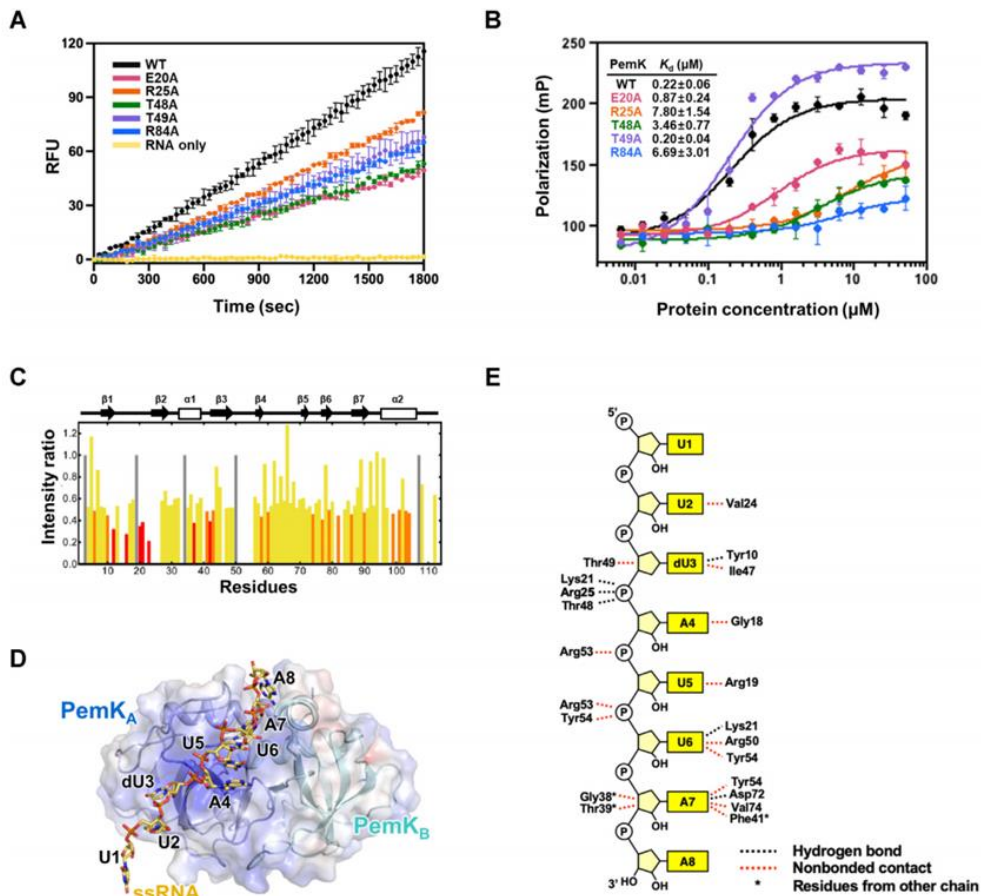


Figure 4. RNA binding and cleavage of PemK. (A) RNase activity assay of PemK WT and its mutants. The colors indicating specific PemK mutants used in the graph are represented in the figure. (B) RNA-binding affinities of PemK WT and its mutants. A fluorescence polarization assay was used to monitor the affinity. (C) The comparison of the NMR peak intensities of residues in PemK upon ssRNA binding (1.0 equivalent) with those without ssRNA binding was plotted according to residue number. The secondary structural elements of PemK are shown above the plot. (D) ssRNA-bound PemK dimer structure produced by the HADDOCK 2.2 webserver. The PemK dimer is represented in cartoon and surface views, and the ssRNA is shown as a stick model. The ssRNA-bound region of PemK exhibited a positively charged distribution. (E) NUCPLOT diagram of contacts between ssRNA and PemK. Black and red dotted lines represent hydrogen bonds and nonbonded contacts ($<3.35 \text{ \AA}$), respectively. Residues of chain B are marked with ‘

3.4. The *S. aureus* PemI monomer neutralizes the PemK dimer by forming a structural complex

To reveal the mechanism underlying the neutralization of PemK by PemI at the molecular level, we performed extensive crystallization of the PemIK protein using a number of constructs, including full-length PemI. After X-ray experiments on various crystal samples, we successfully found that crystallization between the truncated construct Lys57–Ile89 of PemI and the full-length PemK led to the clear observation of electron density from both protein crystals. The solved structure of PemK in complex with PemI was refined at a resolution of 2.00 Å (Table 1). The asymmetric unit comprises three PemI monomers (chains C, F, and I), three PemK dimers (chains A/B, D/E, and G/H), 13 sulfate ions, and one glycerol molecule.

The structure of the PemK monomer from the PemIK complex has the same secondary structural composition observed in the PemK structure without PemI. The structure of the PemI monomer comprises one α -helix (α 1, residues 60–70) (Figure 5A). The interface of two PemI monomers has only one hydrophobic interaction from each Phe67 residue. The antitoxin PemI binds tightly to the toxin PemK dimer with an interface area of $\sim 1,920$ Å². The intrinsically disordered C-terminal region of PemI is aligned along the concave surface between PemK dimers (Figure 5A). In the PemI-PemK interface, the side-chain atoms of residues Phe67, Tyr74, Trp81, Val85, and Ile89 of PemI interact with the hydrophobic region of PemK (Figure 5B). Residues from Tyr74 to Ile79 of PemI form hydrogen bonds and salt bridges extensively with hydrophilic residues in the dimerization surface of the PemK dimer (Figure 5B). In particular, Arg77, Asp80, and Arg84 from chains A and B of PemK form hydrophilic interactions with PemI.

There is no known PemIK complex in other species. Therefore, three complex structures, MazEF from *E. coli* (PDB code 1UB4) (53), MazEF from *B. subtilis* (PDB code E7) (46), and MazEF4 from *M. tuberculosis* (PDB code 5XE3) (54), were compared with the PemIK complex, as shown in Figure 5C. Interestingly,

each antitoxin showed a dissimilar binding mode with its cognate toxin protein, although the three toxin proteins shared a highly similar structural architecture. Among the three compared complexes, the binding mode of *S. aureus* PemI was similar to that of *E. coli* MazE. In both *S. aureus* PemI and *E. coli* MazE, one short α -helix and a long disordered C-terminal coil participated in toxin binding by covering the dimerization interface of the toxin. According to the sequence-based structural motif, the antitoxins *S. aureus* PemI and *E. coli* MazE contain the SpoVT-AbrB domain, while *B. subtilis* MazE and *M. tuberculosis* MazE4 contain a ribbon-helix-helix domain.

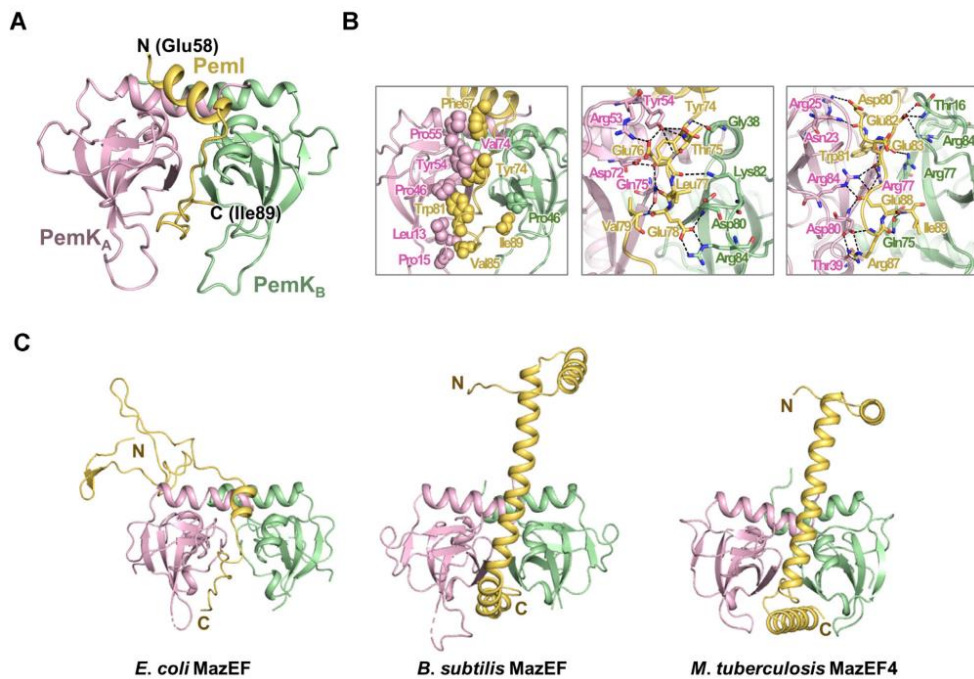


Figure 5. Overall structure of the PemIK complex. (A) Overall structure of PemIK. The PemIK complex, composed of two PemK dimers and one PemI monomer (residues from Lys57 to Ile89), is shown. (B) Interactions between the PemK dimer and PemI monomer. Residues (shown as spheres) contributing to hydrophobic interactions in the PemIK complex are shown in the left rectangle. The residues involved in hydrogen bonds within the PemIK complex are indicated in the middle and right boxes. Hydrogen bonds are shown as black dashes. (C)

Homologs of the PemIK complex. The toxin dimers [monomer A (pink) and monomer B (light green)] and antitoxin monomer (yellow) are represented.

3.5. Loop L12 in PemK plays a decisive role in the formation of the PemIK complex

The interfaces of the PemK dimer in the PemI-neutralized PemK dimer (PemK_{open}) largely deviated from those in the PemK dimer without PemI (PemK_{closed}). The interface area of PemK_{open} was $\sim 1,160 \text{ \AA}^2$, while that of PemK_{closed} was $\sim 1,720 \text{ \AA}^2$. This difference might have originated from the conformational change and movement of L12 of PemK upon PemI binding, which causes structural rearrangement of PemK by switching to the PemK_{closed} conformation from PemK_{open} (Figure 6A). In PemK_{closed}, loop L12 adopts a ‘closed form’ by interacting with residues on L67 and can be involved in RNA substrate binding (Figure 6A).

The conformational change from PemK_{open} to PemK_{closed} is followed by the striking preference for a cis-peptide bond between Asn14 and Pro15 (Figures 6B and 6C). The cis-peptide is observed only in the PemK_{closed}, driving intra- and inter-protein interactions around L12 in a specific way that determines the ‘closed’ conformation, with accommodation of PemI binding. In the PemK_{closed}, Pro15 in PemK makes extensive hydrophilic interactions with Asp12, Asn14, and Arg84 and hydrophobic interactions with Leu13, Leu79, and Pro15', leading to zipping up of the PemI-binding site with more interactions of Thr39/Asp80/Arg84 (PemK_A) and Arg19/Glu20 (PemK_B) (Figure 6B). In the open form of PemK_B, Pro15 forms hydrophilic intermolecular contacts with Thr16, Arg19, and Arg84, leading Asn14 to have extensive hydrophilic interactions with Asp12, Lys21, Asn23, and Arg84 (PemI). Pro15 in PemK_A interacts with Asp12, Asn14, and Thr16 in a hydrophilic manner and makes hydrophobic contacts with Leu13 (Figure 6B).

Interestingly, we observed that PemI mimics the L12 gate in PemK by

replacing the L12 residues of PemK with the residues of PemI when we superimposed PemK_{open} and PemK_{closed} of the PemK structures. Instead of Glu20 in PemK, Glu78 in PemI interacts with Asp80 and Arg84 in PemK. Arg87 in PemI interacts with Thr39 instead of Arg19 in PemK. These two residues of PemI occupy a nearly identical position in L12 of PemK, forming an ‘open’ conformation of PemK (Figure 6C). By forming new interactions between PemI and PemK, Arg25 and Arg84, which affect the RNase activity of PemK, were blocked by hydrophilic interactions with neighboring PemI residues, resulting in the neutralization of PemK toxicity. In addition to the large conformational change in loop L12, slight movements in loop L34 and loop L67 of PemK were also observed upon PemI binding. The movement of loops outward, away from PemI, would result from not only the interaction of PemK residues with PemI but also the flexible nature of the loop regions.

To monitor the dynamic property of PemIK, MD simulations for the PemIK complex were performed. The overall numbers of contacts between PemK and antitoxin PemI have been maintained and the significant variations of RMSD and radius of gyration for the PemIK structure were not shown during 300 ns simulation. Additionally, RMSF on L12 in the structure of PemIK complex (PemK_{open}) was distinctively increased compared to those in PemK (PemK_{closed}). These results indicate that L12 of PemK_{open} is more dynamic than L12 of PemK_{closed} with a flexibility increase. On the other hand, the significant decrease of RMSF at L34 of chain A observed in the structure of PemIK revealed that the region becomes more stable upon binding to PemI.

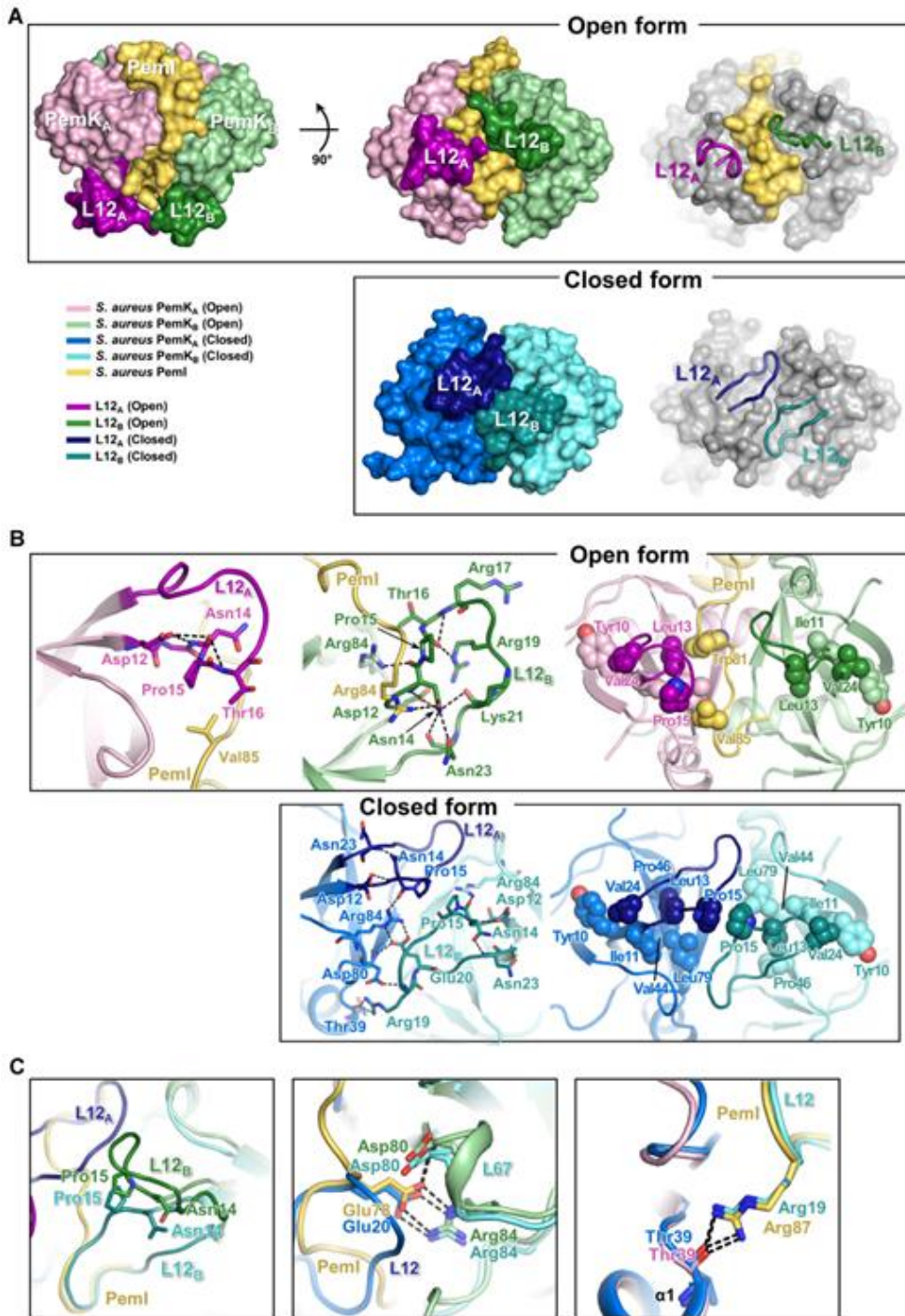


Figure 6. Conformational change of PemK upon PemI binding. (A) PemK and PemIK complex structures in surface view. In the open form of PemK in the PemIK complex, toxins are represented in pink (monomer A) and light green (monomer B). In the closed form, two PemK monomers are colored light blue

(monomer A) and light cyan (monomer B). The antitoxin PemI is represented in yellow. The L12 loops of PemK are highlighted in darker colors (in PemK_{open}, magenta, and green; in the closed form, dark blue and cyan). When PemI binds to PemK, the L12 loops of PemK undergo conformational changes from PemK_{closed} to PemK_{open}. (B) Difference in peptide bonds between Asn14 and Pro15. The residues contributing to hydrophilic interactions are shown with each interaction (black dashes). The residues related to hydrophobic interactions are indicated as spheres. (C) Replacement of PemK residues by PemI residues. Some key residues involved in PemK dimerization are replaced by PemI residues in the PemIK complex structure. The hydrogen bonds in the PemK dimer and PemIK complex are shown in black dashes.

Chapter 4. Conclusion

The *S. aureus* PemIK TA module was first discovered in the low-copy-number plasmid R100. The two corresponding genes located near the replication origin are involved in the stable maintenance of R100. In the genus *Staphylococcus*, a recent study revealed, based on bioinformatics analyses of protein sequences, that the *pemIK* locus is located in not only plasmids but also chromosomes (28).

In this study, we present PemK and PemI-neutralized PemK structures and detailed mechanistic evidence regarding PemK activity and the interference of PemI. The results show that PemK-related proteins, exhibiting a common structural fold, possess their own ways to conduct physiological activities in each organism. In particular, we reveal the importance of the long loop L12 and a large conformational change in L12, which was confirmed by structural comparison between PemK and the PemIK complex. Additionally, MD simulation results also support the flexible property of L12 of PemK. L12 of PemK may play a gating role for PemI antitoxin binding. One of the findings among PemK homologs was the flexibility and length of loops L34, L45, and L67. Additionally, a different distribution of positively charged residues in the crevices on the PemK surface also exists. These characteristics of toxin proteins might determine the conformation for binding the specific RNA or antitoxin.

Several previous studies have revealed the catalytic residues of PemK homologs. In MoxT from *B. anthracis*, His59 and Glu78 were predicted to be the catalytic acid-base couple (55). In Kid from *E. coli*, it was reported that RNA cleavage involves uracil 2' OH from RNA, the catalytic acids are Arg73 and His17, and the catalytic base is Asp75 (56). However, these residues were not found to be conserved when sequence alignment of PemK with its homologs was performed. Other residues, namely, Arg25 and Thr48 in PemK from *S. aureus*, are conserved as Arg25 and Thr48 in MazF from *B. subtilis* and as Arg29 and Thr52 in MazF

from *E. coli*. In MazF from *B. subtilis*, Arg25 is predicted to stabilize the cleavage of the P-O bond (46). In MazF from *E. coli*, Arg29 acts as both a general acid and general base, and Thr52 acts as a stabilizing residue (49). Our comparative analysis indicates that PemK from *S. aureus* may also be involved in mRNA cleavage mediated by acid-base catalysis of residues Arg25 and Thr48. Structural and functional studies on PemK from *S. aureus* revealed that Arg25 and Thr48 play a crucial role in PemK activity in addition to Arg84. It is hypothesized that Arg25 acts as both a general acid and base, and Thr48 stabilizes the transition state in the catalyzed reaction. This involvement of an Arg residue has been shown in other homologs, such as *E. coli* MazF and *B. subtilis* MazF (46,49). Interestingly, Arg84 was presented as a key residue in a previous study (17). Arg84 shows no direct interaction with ssRNA, the Arg84Ala mutant exhibited decreased RNase activity and RNA binding affinity. This essential role of Arg84 might originate from the involvement of hydrogen bonds in maintaining the ‘closed form’, which is catalytically optimal for RNA substrates.

As ribosome-independent RNases, PemK and its homologs recognize specific mRNA sequences. The most notable function of PemK is that it recognizes and cleaves specific tetrad mRNA sequences containing U↓AUU. The RNA sequence “UAUU” could be a codon or anticodon that may be further translated to Tyr or Ile. This selective degradation of transcripts and the subsequent growth inhibition demonstrate the toxicity of PemK in *S. aureus* (17). Inhibition of ribosomal-independent RNase activity of a toxin by its cognate antitoxin can be achieved by the formation of a TA complex, which thoroughly blocks mRNA binding by the toxin. According to the PemI-neutralized PemK structure, an α -helical toxin-binding motif of PemI causes conformational rearrangement of PemK from a ‘closed form’ to an ‘open form’ by binding to the active site residues.

In recent studies, structure-based designed small molecules or peptides that disrupt the TA complexes and induce the artificial activation of toxin resulting in cell death were discovered (57-59). Besides these strategies, engineered toxin-

intein was studied as antimicrobials for the targeted killing of pathogens (60). Our study provides structural information on the toxin protein PemK that will enable researchers to discover inhibitors in the form of pseudopeptides or small molecules. The potential inhibitors could trigger perpetual toxin activation, leading to cell death of bacterial pathogens such as *S. aureus*.

References

1. Ogura, T. and Hiraga, S. (1983) Mini-F plasmid genes that couple host cell division to plasmid proliferation. *Proc. Natl. Acad. Sci. U.S.A.*, **80**, 4784–4788.
2. Holm, L. and Rosenstrom, P. (2010) Dali server: conservation mapping in 3D. *Nucleic Acids Res.*, **38**, W545–549.
3. Yarmolinsky, M.B. (1995) Programmed cell death in bacterial populations. *Science*, **267**, 836–837.
4. Engelberg-Kulka, H., Amitai, S., Kolodkin-Gal, I. and Hazan, R. (2006) Bacterial programmed cell death and multicellular behavior in bacteria. *PLoS Genet.*, **2**, 1518–1526.
5. Yamaguchi, Y., Park, J.H. and Inouye, M. (2011) Toxin-antitoxin systems in bacteria and archaea. *Annu. Rev. Genet.*, **45**, 61–79.
6. Kang, S.M., Kim, D.H., Jin, C.L. and Lee, B.J. (2018) A systematic overview of type II and III toxin-antitoxin systems with a focus on druggability. *Toxins*, **10**, 515.
7. Page, R. and Peti, W. (2016) Toxin-antitoxin systems in bacterial growth arrest and persistence. *Nat. Chem. Biol.*, **12**, 208–214.
8. Cook, G.M., Robson, J.R., Frampton, R.A., McKenzie, J., Przybilski, R., Fineran, P.C. and Arcus, V.L. (2013) Ribonucleases in bacterial toxin-antitoxin systems. *Biochim. Biophys. Acta*, **1829**, 523–531.
9. Yamaguchi, Y. and Inouye, M. (2011) Regulation of growth and death in *Escherichia coli* by toxin-antitoxin systems. *Nat. Rev. Microbiol.*, **9**, 779–790.
10. Williams, J.J. and Hergenrother, P.J. (2012) Artificial activation of toxin-antitoxin systems as an antibacterial strategy. *Trends Microbiol.*, **20**, 291–298.

11. Pandey, D.P. and Gerdes, K. (2005) Toxin-antitoxin loci are highly abundant in free-living but lost from host-associated prokaryotes. *Nucleic Acids Res.*, **33**, 966–976.
12. Brown, J.M. and Shaw, K.J. (2003) A novel family of *Escherichia coli* toxin-antitoxin gene pairs. *J. Bacteriol.*, **185**, 6600–6608.
13. Schuster, C.F. and Bertram, R. (2016) Toxin-antitoxin systems of *Staphylococcus aureus*. *Toxins*, **8**, 140.
14. Zhu, L., Inoue, K., Yoshizumi, S., Kobayashi, H., Zhang, Y., Ouyang, M., Kato, F., Sugai, M. and Inouye, M. (2009) *Staphylococcus aureus* MazF specifically cleaves a pentad sequence, UACAU, which is unusually abundant in the mRNA for pathogenic adhesive factor SraP. *J. Bacteriol.*, **191**, 3248–3255.
15. Yoshizumi, S., Zhang, Y., Yamaguchi, Y., Chen, L., Kreiswirth, B.N. and Inouye, M. (2009) *Staphylococcus aureus* YoeB homologues inhibit translation initiation. *J. Bacteriol.*, **191**, 5868–5872.
16. Tsuchimoto, S., Ohtsubo, H. and Ohtsubo, E. (1988) Two genes, pemK and pemI, responsible for stable maintenance of resistance plasmid R100. *J. Bacteriol.*, **170**, 1461–1466.
17. Bukowski, M., Lyzen, R., Helbin, W.M., Bonar, E., Szalewska-Palasz, A., Wegrzyn, G., Dubin, G., Dubin, A. and Wladyka, B. (2013) A regulatory role for *Staphylococcus aureus* toxin-antitoxin system PemIKSa. *Nat. Commun.*, **4**, 2012.
18. Sengupta, M. and Austin, S. (2011) Prevalence and significance of plasmid maintenance functions in the virulence plasmids of pathogenic bacteria. *Infect. Immun.*, **79**, 2502–2509.
19. Nordstrom, K. and Austin, S.J. (1989) Mechanisms that contribute to the stable segregation of plasmids. *Annu. Rev. Genet.*, **23**, 37–69.

20. Zhang, J., Zhang, Y., Zhu, L., Suzuki, M. and Inouye, M. (2004) Interference of mRNA function by sequence-specific endoribonuclease PemK. *J. Biol. Chem.*, **279**, 20678–20684.
21. DeLeo, F.R., Diep, B.A. and Otto, M. (2009) Host defense and pathogenesis in *Staphylococcus aureus* infections. *Infect. Dis. Clin. North Am.*, **23**, 17–34.
22. Dreisbach, A., van Dijl, J.M. and Buist, G. (2011) The cell surface proteome of *Staphylococcus aureus*. *Proteomics*, **11**, 3154–3168.
23. Schlievert, P.M., Strandberg, K.L., Lin, Y.C., Peterson, M.L. and Leung, D.Y. (2010) Secreted virulence factor comparison between methicillin-resistant and methicillin-sensitive *Staphylococcus aureus*, and its relevance to atopic dermatitis. *J. Allergy Clin. Immunol.*, **125**, 39–49.
24. Torres, V.J., Attia, A.S., Mason, W.J., Hood, M.I., Corbin, B.D., Beasley, F.C., Anderson, K.L., Stauff, D.L., McDonald, W.H., Zimmerman, L.J. *et al.* (2010) *Staphylococcus aureus* fur regulates the expression of virulence factors that contribute to the pathogenesis of pneumonia. *Infect. Immun.*, **78**, 1618–1628.
25. Mir, D.A. and Balamurugan, K. (2019) Global proteomic response of *Caenorhabditis elegans* against PemK_{Sa} toxin. *Front. Cell Infect. Microbiol.*, **9**, 172.
26. Bleriot, I., Blasco, L., Delgado-Valverde, M., Gual de Torella, A., Ambroa, A., Fernandez-Garcia, L., Lopez, M., Oteo-Iglesias, J., Wood, T.K., Pascual, A. *et al.* (2020) Mechanisms of tolerance and resistance to chlorhexidine in clinical strains of *Klebsiella pneumoniae* producers of carbapenemase: Role of New Type II Toxin-Antitoxin System, PemIK. *Toxins*, **12**, 566.
27. Chi, X., Chang, Y., Li, M., Lin, J., Liu, Y., Li, C., Tang, S. and Zhang, J. (2018) Biochemical characterization of mt-PemIK, a novel toxin-antitoxin system in *Mycobacterium tuberculosis*. *FEBS Lett.*, **592**, 4039–4050.

28. Bukowski, M., Hyz, K., Janczak, M., Hydzik, M., Dubin, G. and Wladyka, B. (2017) Identification of novel mazEF/pemIK family toxin-antitoxin loci and their distribution in the *Staphylococcus* genus. *Sci. Rep.*, **7**, 13462.
29. Takeuchi, S., Kinoshita, T., Kaidoh, T. and Hashizume, N. (1999) Purification and characterization of protease produced by *Staphylococcus aureus* isolated from a diseased chicken. *Vet. Microbiol.*, **67**, 195–202.
30. Otwinowski, Z. and Minor, W. (1997) Processing of X-ray diffraction data collected in oscillation mode. *Methods Enzymol.*, **276**, 307–326.
31. Kabsch, W. (2010) XDS. *Acta Crystallogr. Sect. D: Biol. Crystallogr.*, **66**, 125–132.
32. McCoy, A.J., Grosse-Kunstleve, R.W., Adams, P.D., Winn, M.D., Storoni, L.C. and Read, R.J. (2007) Phaser crystallographic software. *J. Appl. Crystallogr.*, **40**, 658–674.
33. Hargreaves, D., Santos-Sierra, S., Giraldo, R., Sabariegos-Jareno, R., de la Cueva-Mendez, G., Boelens, R., Diaz-Orejas, R. and Rafferty, J.B. (2002) Structural and functional analysis of the kid toxin protein from *E. coli* plasmid R1. *Structure*, **10**, 1425–1433.
34. Adams, P.D., Afonine, P.V., Bunkoczi, G., Chen, V.B., Davis, I.W., Echols, N., Headd, J.J., Hung, L.W., Kapral, G.J., Grosse-Kunstleve, R.W. *et al.* (2010) PHENIX: a comprehensive Python-based system for macromolecular structure solution. *Acta Crystallogr. Sect. D: Biol. Crystallogr.*, **66**, 213–221.
35. Brunger, A.T. (1992) Free R value: a novel statistical quantity for assessing the accuracy of crystal structures. *Nature*, **355**, 472–475.
36. Emsley, P., Lohkamp, B., Scott, W.G. and Cowtan, K. (2010) Features and development of Coot. *Acta Crystallogr. Sect. D: Biol. Crystallogr.*, **66**, 486–501.

37. Murshudov, G.N., Vagin, A.A. and Dodson, E.J. (1997) Refinement of macromolecular structures by the maximum-likelihood method. *Acta Crystallogr. Sect. D: Biol. Crystallogr.*, **53**, 240-255.
38. Winn, M.D., Ballard, C.C., Cowtan, K.D., Dodson, E.J., Emsley, P., Evans, P.R., Keegan, R.M., Krissinel, E.B., Leslie, A.G., McCoy, A. *et al.* (2011) Overview of the CCP4 suite and current developments. *Acta Crystallogr. Sect. D: Biol. Crystallogr.*, **67**, 235–242.
39. Chen, V.B., Arendall, W.B., 3rd, Headd, J.J., Keedy, D.A., Immormino, R.M., Kapral, G.J., Murray, L.W., Richardson, J.S. and Richardson, D.C. (2010) MolProbity: all-atom structure validation for macromolecular crystallography. *Acta Crystallogr. Sect. D: Biol. Crystallogr.*, **66**, 12–21.
40. Krissinel, E. and Henrick, K. (2007) Inference of macromolecular assemblies from crystalline state. *J. Mol. Biol.*, **372**, 774–797.
41. Tina, K.G., Bhadra, R. and Srinivasan, N. (2007) PIC: Protein Interactions Calculator. *Nucleic Acids Res.*, **35**, 473–476.
42. Delaglio, F., Grzesiek, S., Vuister, G.W., Zhu, G., Pfeifer, J. and Bax, A. (1995) NMRPipe: a multidimensional spectral processing system based on UNIX pipes. *J. Biomol. NMR*, **6**, 277–293.
43. Johnson, B.A. and Blevins, R.A. (1994) NMR View: A computer program for the visualization and analysis of NMR data. *J. Biomol. NMR*, **4**, 603–614.
44. Lundblad, J.R., Laurance, M. and Goodman, R.H. (1996) Fluorescence polarization analysis of protein-DNA and protein-protein interactions. *Mol. Endocrinol.*, **10**, 607–612.
45. van Zundert, G.C.P., Rodrigues, J., Trellet, M., Schmitz, C., Kastiris, P.L., Karaca, E., Melquiond, A.S.J., van Dijk, M., de Vries, S.J. and Bonvin, A. (2016) The HADDOCK2.2 web server: user-friendly integrative modeling of biomolecular complexes. *J. Mol. Biol.*, **428**, 720–725.

46. Simanshu, D.K., Yamaguchi, Y., Park, J.H., Inouye, M. and Patel, D.J. (2013) Structural basis of mRNA recognition and cleavage by toxin MazF and its regulation by antitoxin MazE in *Bacillus subtilis*. *Mol. Cell*, **52**, 447–458.
47. Abraham, M.J., Murtola, T., Schulz, R., Páll, S., Smith, J.C., Hess, B. and Lindahl, E. (2015) GROMACS: High performance molecular simulations through multi-level parallelism from laptops to supercomputers. *SoftwareX*, **1**, 19–25.
48. Valdes-Tresanco, M.S., Valdes-Tresanco, M.E., Valiente, P.A. and Moreno, E. (2021) gmx_MMPBSA: A new tool to perform end-state free energy calculations with GROMACS. *J. Chem. Theory Comput.*, **17**, 6281–6291.
49. Zorzini, V., Mernik, A., Lah, J., Sterckx, Y.G., De Jonge, N., Garcia-Pino, A., De Greve, H., Versees, W. and Loris, R. (2016) Substrate recognition and activity regulation of the *Escherichia coli* mRNA endonuclease MazF. *J. Biol. Chem.*, **291**, 10950–10960.
50. Zorzini, V., Buts, L., Sleutel, M., Garcia-Pino, A., Talavera, A., Haesaerts, S., De Greve, H., Cheung, A., van Nuland, N.A. and Loris, R. (2014) Structural and biophysical characterization of *Staphylococcus aureus* SaMazF shows conservation of functional dynamics. *Nucleic Acids Res.*, **42**, 6709–6725.
51. Verma, S., Kumar, S., Gupta, V.P., Gourinath, S., Bhatnagar, S. and Bhatnagar, R. (2014) Structural basis of *Bacillus anthracis* MoxXT disruption and the modulation of MoxT ribonuclease activity by rationally designed peptides. *J. Biomol. Struct. Dyn.*, **33**, 606–624.
52. Barbas, A., Matos, R.G., Amblar, M., Lopez-Vinas, E., Gomez-Puertas, P. and Arraiano, C.M. (2009) Determination of key residues for catalysis and RNA cleavage specificity: one mutation turns RNase II into a "SUPER-ENZYME". *J. Biol. Chem.*, **284**, 20486–20498.

53. Kamada, K., Hanaoka, F. and Burley, S.K. (2003) Crystal structure of the MazE/MazF complex: molecular bases of antidote-toxin recognition. *Mol.Cell*, **11**, 875–884.
54. Ahn, D.H., Lee, K.Y., Lee, S.J., Park, S.J., Yoon, H.J., Kim, S.J. and Lee, B.J. (2017) Structural analyses of the MazEF4 toxin-antitoxin pair in *Mycobacterium tuberculosis* provide evidence for a unique extracellular death factor. *J. Biol. Chem.*, **292**, 18832–18847.
55. Agarwal, S., Mishra, N.K., Bhatnagar, S. and Bhatnagar, R. (2010) PemK toxin of *Bacillus anthracis* is a ribonuclease: an insight into its active site, structure, and function. *J. Biol. Chem.*, **285**, 7254–7270.
56. Kamphuis, M.B., Bonvin, A.M., Monti, M.C., Lemonnier, M., Munoz-Gomez, A., van den Heuvel, R.H., Diaz-Orejas, R. and Boelens, R. (2006) Model for RNA binding and the catalytic site of the RNase Kid of the bacterial parD toxin-antitoxin system. *J.Mol.Biol.*, **357**, 115–126.
57. Kang, S.M., Jin, C., Kim, D.H., Lee, Y. and Lee, B.J. (2020) Structural and functional study of the *Klebsiella pneumoniae* VapBC toxin-antitoxin system, including the development of an inhibitor that activates VapC. *J. Med. Chem.*, **63**, 13669–13679.
58. Kang, S.M., Jin, C., Kim, D.H., Park, S.J., Han, S.W. and Lee, B.J. (2021) Structure-based design of peptides that trigger *Streptococcus pneumoniae* cell death. *FEBS J.*, **288**, 1546–1564.
59. Kang, S.M., Moon, H., Han, S.W., Kim, B.W., Kim, D.H., Kim, B.M. and Lee, B.J. (2021) Toxin-activating stapled peptides discovered by structural analysis were identified as new therapeutic candidates that trigger antibacterial activity against *Mycobacterium tuberculosis* in the *Mycobacterium smegmatis* model. *Microorganisms*, **9**. 568.
60. López-Igual, R., Bernal-Bayard, J., Rodríguez-Paton, A., Ghigo, J.-M. and Mazel, D. (2019) Engineered toxin–intein antimicrobials can selectively

target and kill antibiotic-resistant bacteria in mixed populations. *Nat. Biotechnol.*, **37**, 755–760.

61. Madeira, F., Park, Y.M., Lee, J., Buso, N., Gur, T., Madhusoodanan, N., Basutkar, P., Tivey, A.R.N., Potter, S.C., Finn, R.D. *et al.* (2019) The EMBL-EBI search and sequence analysis tools APIs in 2019. *Nucleic Acids Res.*, **47**, 636–641.
62. Robert, X. and Gouet, P. (2014) Deciphering key features in protein structures with the new ENDscript server. *Nucleic Acids Res.*, **42**, 320–324.

국문초록

Staphylococcus aureus 유래 PemIK TA system 단백질 복합체의 구조 및 기능 연구

백 성 민

서울대학교 대학원

약학과 약학전공

황색포도상구균은 세계적으로 알려진 병원균으로 피부 혹은 호흡계통에 존재하여 화농성 관절염, 심내막염, 폐렴 등을 일으킨다. 황색포도상구균은 주로 항생제를 통해 치료하며, 주로 사용되는 항생제는 glycopeptide 계열 항생제인 vancomycin과 beta-lactam 계열 항생제인 methicillin이다. 그러나 항생제 과다사용으로 인한 항생제 내성균주인 Methicillin-resistant Staphylococcus aureus (MRSA), Vancomycin-resistant Staphylococcus aureus (VRSA)의 출현으로 항생제 내성균 감염에 대한 치료가 어려운 실정이다. 따라서 본 연구진은 새로운 약물 기전으로써 황색포도상구균의 독소-항독소 (Toxin-antitoxin) 시스템

연구를 진행하였다.

독소-항독소 시스템은 균의 자가사멸을 유도하거나 성장을 억제하는 toxin과 상응하는 antitoxin 유전자를 구성하는 유전적 모듈을 말한다. 이 시스템은 오직 원핵생물에 존재하기 때문에 새로운 기전의 약물 개발로 매력적인 타겟이며 최근 활발한 연구가 진행되고 있다. 본 연구진은 황색포도상구균 typeII 독소-항독소 시스템 중 최근 밝혀진 Plasmid emergency maintenance inhibitor or killing (PemIK)에 주목하였다. PemIK 복합체는 endonuclease 활성을 가진 toxin 단백질 PemK와 toxin 단백질의 활성을 저해하는 antitoxin 단백질 PemI로 구성되어 있으며 주요한 세포 기능을 조절한다. 본 연구에서는 황색포도상구균의 PemK와 PemIK 복합체의 X-선 삼차원 결정 구조를 규명하였다. 그 구조를 통해 PemK의 RNase SH3-like fold를 밝혀냈고, PemI에 따른 PemK의 conformational change를 분석하여 PemIK 복합체 형성을 통한 PemK의 기능 저해를 확인했다. 또한 생물물리학적, 생화학적인 분석을 통해 PemK 활성에 중요한 잔기들을 밝혀냈다. 이러한 연구는 PemIK의 구조를 기반한 이해와 복합체 형성을 조절하는 펩타이드 및 저분자 물질 개발을 통해 항생제 내성에 대항하는 혁신 치료제 개발을 위한 좋은 플랫폼으로서 작용할 수 있다.

주요어 : 황색포도상구균, 항생제 내성, MRSA, 독소-항독소 (Toxin-antitoxin) 시스템, PemIK, X선 삼차원 결정 구조, Conformational change

학번 : 2020-28855